CrossMark

RESEARCH ARTICLE

Optimization of planar PIV-based pressure estimates in laminar and turbulent wakes

Jeffrey McClure[1] · Serhiy Yarusevych[1]

Abstract The performance of four pressure estimation techniques using Eulerian material acceleration estimates from planar, two-component Particle Image Velocimetry (PIV) data were evaluated in a bluff body wake. To allow for the ground truth comparison of the pressure estimates, direct numerical simulations of flow over a circular cylinder were used to obtain synthetic velocity fields. Direct numerical simulations were performed for $Re_D = 100$, 300, and 1575, spanning laminar, transitional, and turbulent wake regimes, respectively. A parametric study encompassing a range of temporal and spatial resolutions was performed for each Re_D. The effect of random noise typical of experimental velocity measurements was also evaluated. The results identified optimal temporal and spatial resolutions that minimize the propagation of random and truncation errors to the pressure field estimates. A model derived from linear error propagation through the material acceleration central difference estimators was developed to predict these optima, and showed good agreement with the results from common pressure estimation techniques. The results of the model are also shown to provide acceptable first-order approximations for sampling parameters that reduce error propagation when Lagrangian estimations of material acceleration are employed. For pressure integration based on planar PIV, the effect of flow three-dimensionality was also quantified, and shown to be most pronounced at higher Reynolds numbers downstream of the vortex formation region, where dominant vortices undergo substantial three-dimensional deformations. The results of the present study provide a priori recommendations for the use of pressure

estimation techniques from experimental PIV measurements in vortex dominated laminar and turbulent wake flows.

1 Introduction

The utility of spatio-temporally resolved fluid pressure estimations from time-resolved particle image velocimetry (TR-PIV) measurements (van Oudheusden 2013) has been demonstrated in turbulent boundary layers (Ghaemi et al. 2012; Pröbsting et al. 2013; Laskari et al. 2016; Schneiders et al. 2016), jets (de Kat et al. 2013), bluff-body wakes (de Kat and van Oudheusden 2012; Dabiri et al. 2014; Fujisawa et al. 2005; van Oudheusden et al. 2007; McClure and Yarusevych 2016), subsonic (Auteri et al. 2015; van Oudheusden et al. 2006, 2007; Violato et al. 2011) and supersonic aerofoils (van Oudheusden et al. 2007), aircraft propellers (Ragni et al. 2012), pulsatile diffusers (Charonko et al. 2010), the region surrounding a rising bubble (Hosokawa et al. 2003), cavity flows (Liu and Katz 2006), and other flow configurations (Murai et al. 2007). Estimated pressure fields can be used in conjunction with measured velocity fields to extract time-resolved loadings on immersed structures (van Oudheusden et al. 2007; Tronchin et al. 2015), establishing a minimally intrusive methodology for the measurement of both fluid pressure and structural loading. A number of methodologies have emerged from the results of individual studies, however, a clear consensus on an optimum has not yet been reached, and may be flow or setup dependent (Charonko et al. 2010; van Oudheusden 2013).

To estimate fluid pressure ($p(x, y, t)$), the instantaneous velocity fields ($u_i(x, y, t)$) obtained from two-component

✉ Jeffrey McClure
  jejmcclu@uwaterloo.ca

[1] University of Waterloo, Waterloo, ON N2L3G1, Canada

Springer

TR-PIV measurements are used to calculate the planar pressure gradients from the Navier–Stokes equations:

$$\frac{\partial p}{\partial x} = -\rho\left(\frac{\partial u}{\partial t} + u\frac{\partial u}{\partial x} + v\frac{\partial u}{\partial y} + w\frac{\partial u}{\partial z}\right) + \mu\left(\frac{\partial^2 u}{\partial x^2} + \frac{\partial^2 u}{\partial y^2} + \frac{\partial^2 u}{\partial z^2}\right) \tag{1}$$

$$\frac{\partial p}{\partial y} = -\rho\left(\frac{\partial v}{\partial t} + u\frac{\partial v}{\partial x} + v\frac{\partial v}{\partial y} + w\frac{\partial v}{\partial z}\right) + \mu\left(\frac{\partial^2 v}{\partial x^2} + \frac{\partial^2 v}{\partial y^2} + \frac{\partial^2 v}{\partial z^2}\right) \tag{2}$$

Since only two velocity components are measured in planar PIV (u, v), terms containing the out-of-plane velocity (w) or out-of-plane derivatives ($\partial/\partial z$) are not evaluated (Baur and Köngeter 1999; Charonko et al. 2010; de Kat and van Oudheusden 2012; Ghaemi et al. 2012). In more general terms, the pressure gradient is related to forces arising from viscous stresses and material acceleration (Eq. 3).

$$\frac{\partial p}{\partial x_i} = \mu\frac{\partial^2 u_i}{\partial x_i^2} - \rho\frac{Du_i}{Dt} \tag{3}$$

The pressure gradient field may then be integrated, using for example one of the following methods proposed in previous studies: (1) Baur and Köngeter (1999) utilized a spatial marching scheme, (2) Liu and Katz (2006) developed an omni-directional line integration technique, (3) Dabiri et al. (2014) proposed an eight-path line integration technique, (4) multiple authors solved the pressure Poisson equation using a standard 5-point discretization (Gurka et al. 1999; Fujisawa et al. 2005; de Kat and van Oudheusden 2012; Blinde et al. 2016) or with an FFT integration (Huhn et al. 2016):

$$\frac{\partial^2 p}{\partial x_i^2} = -\rho\frac{\partial}{\partial x_i}\frac{Du_i}{Dt} \tag{4}$$

simultaneously over the domain, (5) Tronchin et al. (2015) solved local equations for the least squares approximation of the pressure field using an iterative method and (6) multiple authors (Regert et al. 2001; Hosokawa et al. 2003; Jaw et al. 2009) have explored coupling the PIV velocity fields with common CFD algorithms to solve the pressure Poisson equation. Recent developments in tomographic PIV (Elsinga et al. 2006) and three-dimensional particle tracking velocimetry (PTV) (Schanz et al. 2016) allow three-dimensional velocity field characterization inside a volume, further extending the capacity of pressure estimation (Violato et al. 2011; Ghaemi et al. 2012; Neeteson and Rival 2015; Laskari et al. 2016; Schneiders et al. 2016). For volumetric data, Poisson equation based methods are widely used and are relatively computationally inexpensive (Blinde et al. 2016; Huhn et al. 2016). However, the majority of prior work on pressure estimation has been focused on planar velocity measurements, and such measurements are still prevalent.

Accurate estimation of the material acceleration (Du_i/Dt) is vital to any method of pressure estimation, since the viscous terms in Eq. 3 can often be neglected or are relatively small for turbulent flows where the inertial terms dominate (Ghaemi et al. 2012). The material acceleration is typically estimated in either an Eulerian or Lagrangian frame of reference. In the Eulerian frame, the material acceleration is estimated at each grid point using, for example, second order central differences (Gurka et al. 1999) (Eq. 5).

$$\begin{aligned}\frac{Du_i}{Dt}(\mathbf{x}, t) = {}&\frac{u_i(\mathbf{x}, t + \Delta t) - u_i(\mathbf{x}, t - \Delta t)}{2\Delta t} \\ &+ u_i(\mathbf{x}, t)\frac{u_i(\mathbf{x} + \Delta x_i, t) - u_i(\mathbf{x} - \Delta x_i, t)}{2\Delta x}\end{aligned} \tag{5}$$

In the Lagrangian frame, pseudo-tracking methods are used to track a fluid element coincident with each grid point at time t. For example, the material acceleration of the tracked element may be estimated by iteratively determining the trajectory of the element backward and forward in time using Eqs. 6 and 7 (Liu and Katz 2006; de Kat and van Oudheusden 2012; Lynch and Scarano 2014):

$$\mathbf{x}_p^k(t, \tau) = \mathbf{x} + u_i(\mathbf{x}, t)\tau + \frac{1}{2}\frac{Du_i^k}{Dt}(\mathbf{x}, t)\tau^2 \tag{6}$$

$$\frac{Du_i^{k+1}}{Dt}(\mathbf{x}, t) = \frac{u_i(\mathbf{x}_p^k(t, \Delta t), t + \Delta t) - u_i(\mathbf{x}_p^k(t, -\Delta t), t - \Delta t)}{2\Delta t} \tag{7}$$

Methods of material acceleration determination have been found to be subject to differing temporal resolution constraints depending on the advective and rotational nature of the flow (Violato et al. 2011; de Kat and van Oudheusden 2012; Jakobsen et al. 1997; van Oudheusden 2013). Studies of wave phenomena indicated that the Lagrangian approach performs poorly compared to the Eulerian (Jakobsen et al. 1997). Violato et al. (2011) compared errors associated with Eulerian and Lagrangian techniques for flow over a rod–airfoil and found that the upper bound on Δt required to properly sample the convective structures was lower for the Eulerian method compared to the Lagrangian method ($\Delta t_{\text{Lag,max}}/\Delta t_{\text{Eul,max}} \approx 3$). When adhering to this guideline, resulting pressure evaluations showed minor differences between the Eulerian and Lagrangian estimations (Violato et al. 2011). de Kat and van Oudheusden (2012) studied the peak response characteristics of an advecting vortex flow and suggested that the upper bound for Δt scales according to the advective time-scale of the vortices for the Eulerian method, and according to the vortex turn-over time for the Lagrangian method. Hence,

in contrast to the results of Violato et al. (2011), de Kat and van Oudheusden (2012) found that, in the wake of a square cylinder, the pressure estimated using the Lagrangian approach leads to a rapid decrease in correlation with surface microphone measurements at significantly smaller Δt ($\Delta t_{\mathrm{Lag,max}}/\Delta t_{\mathrm{Eul,max}} \approx 0.1$). They recommended bounds on the interrogation window size of $\lambda_x/\mathrm{WS} > 5$ and on the acquisition frequency of $f_{\mathrm{acq}}/f_{\mathrm{flow}} > 10$, where λ_x and f_{flow} are the smallest wavelength and the highest frequency of structures to be resolved in the estimated pressure field.

Important for the experimental application of the techniques are methods to reduce the effect of random error propagation to the material acceleration. Noise reduction in material acceleration estimates can be achieved by reconstructing the fluid parcel trajectories over multiple time realizations (Violato et al. 2011; Novara and Scarano 2013; Pröbsting et al. 2013; Lynch and Scarano 2014), filtering the velocity fields (Charonko et al. 2010; Dabiri et al. 2014), or applying Taylor's frozen field hypothesis for highly convective flows (de Kat et al. 2013; Laskari et al. 2016). With the accuracy of the pressure estimation being dependent on the random errors present in the velocity measurements, the sensitivity of pressure estimation to typical measurement errors becomes an important criterion for the identification of an optimal technique. The omnidirectional, spatial marching, and Poisson solver techniques were compared by Charonko et al. (2010) using analytical solutions for a pulsatile flow and a decaying vortex subject to artificially applied velocity noise. It was concluded that the Poisson equation method performs better for the advective oscillating slot flow, while omni-directional line-integration and spatial marching methods perform better for the rotational vortex flow. Murai et al. (2007) superimposed artificial error onto their experimental results and found the Poisson equation method to be relatively insensitive to velocity field noise compared to the line-integration methods for flow around a Savonious turbine. Using an analytical solution for an advecting vortex, de Kat and van Oudheusden (2012) found negligible differences between the omni-directional technique and the pressure Poisson equation, but inhomogeneous propagation of velocity error led to higher overall error values for the spatial marching method. Recently, Blinde et al. (2016) compared a number of pressure estimation techniques using synthetic data obtained from a zonal detached eddy simulation (ZDES) of an axisymmetric base flow, and showed the superiority of PTV-based material acceleration estimates for computing pressure fields, as well as the benefit of several techniques which implicitly correct the velocity field in the solution for pressure. Some recent studies have attempted to quantify the uncertainty in pressure estimations (ε_{p}) given uncertainties in the velocity field (ε_{u}) (Violato et al. 2011; de Kat and van Oudheusden 2012; de Kat et al. 2013; Laskari et al. 2016; Azijli et al. 2016), focusing on the Poisson equation problem.

Although the analytical framework has yet to be developed fully, multiple studies (Laskari et al. 2016; Charonko et al. 2010; Violato et al. 2011) suggest that optimal temporal and spatial resolutions exist which minimize the resulting pressure error by balancing the truncation error ($\varepsilon_{\mathrm{trunc}}$) of the derivative estimates and the random error propagation ($\varepsilon_{\mathrm{rand}}$) into the pressure integration. In addition, with optimum methodologies apparently dependent on the flow case (Charonko et al. 2010), it is of interest to comprehensively evaluate the performance of common pressure estimation techniques in flows that are representative of practical applications, building on the work performed to date on analytical models of relatively simple flows (Charonko et al. 2010; de Kat and van Oudheusden 2012). The present study considers a circular cylinder in cross-flow, which represents a prototypical flow case in bluff-body aerodynamics encountered in a variety of practical applications. The main objective is to determine an optimal pressure estimation method, as well as associated optimum sampling rates (f_{acq}) and spatial resolutions (WS) of acquired velocity data for pressure estimation in vortex dominated wakes. In addition, the errors associated with utilizing planar velocimetry data in a three-dimensional flow will be quantified. Previous studies have compared errors associated with utilizing planar velocimetry data by comparing planar and volumetric evaluations on experimental data (de Kat and van Oudheusden 2012; Ghaemi et al. 2012) or by sampling analytical solutions on offset planes (Charonko et al. 2010; de Kat and van Oudheusden 2012); however, the error has yet to be globally quantified for a realistic flow case. To provide a reference pressure data for comparison, direct numerical simulations (DNS) are used to simulate experimentally acquired velocity fields. The flows spanning laminar, transitional, and turbulent shedding regimes are subjected to uncorrelated velocity noise to simulate an experimental environment. The results inform on the errors involved in pressure integration from planar PIV data, obtained by common methodologies, and provide recommendations for optimal experimental parameters for minimizing the errors in estimated pressure fields.

2 Methodology

2.1 Direct numerical simulations

Pressure estimation techniques were tested with synthetic PIV data sampled from direct numerical simulations of a circular cylinder in cross flow for $Re_{\mathrm{D}} = 100, 300,$ and 1575. The incompressible Navier–Stokes equations were

solved using a finite volume solver (ANSYS CFX 14.0). The solver uses a second-order, blended finite difference spatial discretization scheme and a second-order backwards Euler implicit time marching scheme. The equations were discretized and solved on a two-dimensional mesh for $Re_D = 100$, since previous experiments and simulations have established that no three dimensional effects are present in the near wake at this Reynolds number (e.g., Persillon and Braza 1998; Williamson 1996). Three-dimensional meshes were used for $Re_D = 300$ and 1575 (Fig. 1).

The mesh is a structured O-type around the cylinder and a structured H-type mesh in the remaining regions (Fig. 1). Such a hybrid mesh configuration is commonly used in numerical studies on cylindrical geometries (e.g., Inoue and Sakuragi 2008; Morton and Yarusevych 2010; McClure et al. 2015). A uniform streamwise velocity ($u = (U_\infty, 0, 0)$) is prescribed at the inlet boundary and an average static pressure of zero is set across the outlet boundary ($\overline{p} = 0$). The no-slip condition ($u = (0, 0, 0)$) is prescribed at the cylinder surface, and the free-slip condition ($u_n = 0, \partial u_t/\partial n = 0$) is imposed on the remaining domain boundaries. Mesh sizing near the surface of the cylinder (Table 1) was ensured to be well below sizing recommendations relative to the Kolomogorov scale (η) recommended by Moin and Mahesh (1998) for DNS of common turbulent flows. The mesh sizing can further be compared to the DNS study of Wissink and Rodi (2008), who employed a second order discretization in space for
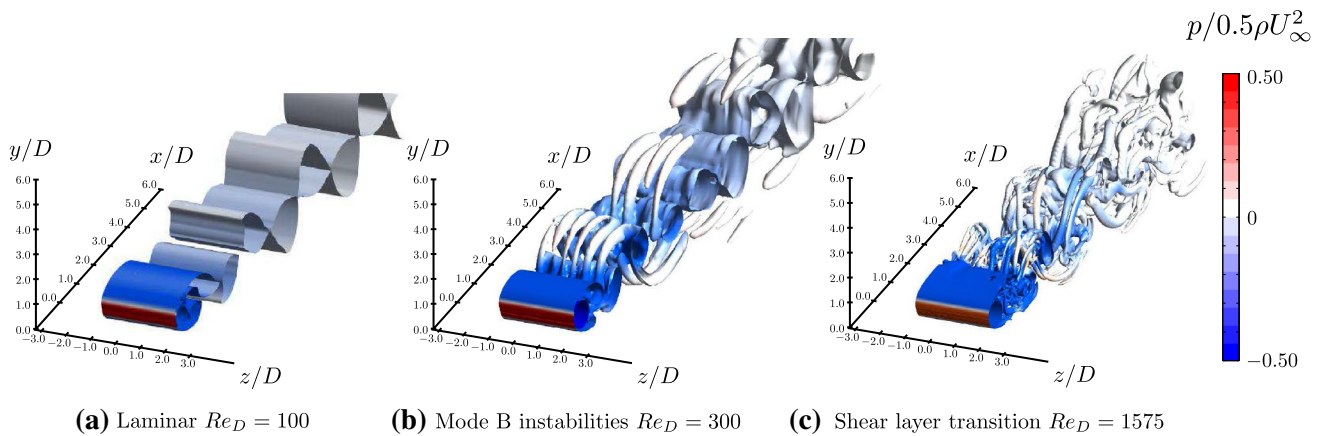
a uniform cylinder at $Re_D = 3300$ and tested five meshes with various levels of refinement. They achieved good convergence, based on wake statistics, with a mesh containing 1.4×10^8 nodes, and utilized similar relative refinement in the circumferential, radial, and spanwise directions (Table 1) as those employed in the current study. Assuming the node count scales approximately with $Re_D^{9/4}$ (Moin and Mahesh 1998), 2.9×10^7 nodes for $Re_D = 1575$ (Table 1) was deemed sufficient. The simulations for $Re_D = 300$ and 1575 were initialized by course mesh simulations which spanned the initial transient of the vortex shedding excitation, and results from the fine mesh simulation were sampled once the fluctuating lift and drag forces reached a quasi-steady state. The instantaneous force data on the cylinder and streamwise velocity data at $x/D = 5$, $y/D = 0.75$ were then collected for a minimum duration of 8 cylinder vortex shedding cycles. The shedding frequency (f_s) was estimated based on a sinusoidal regression of the streamwise velocity data. The results pertaining to the fluctuating lift force (C_L), shedding frequency ($St_D = f_s D/U_\infty$), and mean drag (C_D) are summarized in Table 1 and compared to available experimental data. A comparison with experimental values shows a maximum deviation of 5.6%. The minor deviations between numerical and experimental data in Table 1 are similar to those found in other DNS studies at similar Reynolds numbers (Marzouk et al. 2007; Wissink and Rodi 2008; Zhao and Cheng 2014).

Fig. 1 Hybrid O-type and H-type structured computational mesh, showing the mesh density utilized for $Re_D = 1575$
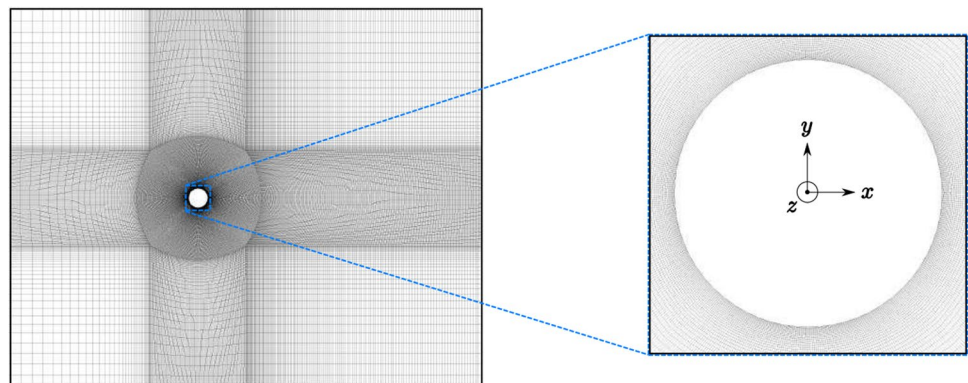
Table 1 Mesh parameters alongside experimental (bold) and numerical results for flow around a circular cylinder

Re_D	Nodes	$\Delta\theta/\eta \times \Delta r/\eta \times \Delta z/\eta$	L_z/D	St_D	$C_{L'}$	C_D
100	1.2×10^5	$0.53 \times 0.08 \times 0$	0	0.167	0.232	1.35
				0.16 (Norberg 2003)	**0.23** (Norberg 2003)	**1.43** (Wieselsberger 1921)
300	1.1×10^6	$1.21 \times 0.66 \times 4.88$	6	0.199	0.438	1.278
				0.20 (Norberg 2003)	**0.46** (Norberg 2003)	**1.24** (Wieselsberger 1921)
1575	2.9×10^7	$1.59 \times 0.71 \times 2.85$	π	0.217	0.043	0.964
				0.21 (Norberg 2003)	**0.045** (Norberg 2003)	**0.95** (Wieselsberger 1921)

$$p/0.5\rho U_\infty^2$$

(a) Laminar $Re_D = 100$ **(b)** Mode B instabilities $Re_D = 300$ **(c)** Shear layer transition $Re_D = 1575$

Fig. 2 Vortex visualizations using the λ_2-criterion ($\lambda_2 = -0.01$) (Jeong and Hussain 1995) for **a** laminar vortex shedding at $Re_D = 100$ (two-dimensional data extruded for comparison), **b** transitional vortex shedding at $Re_D = 300$, and **c** turbulent vortex shedding at $Re_D = 1575$

The results are illustrated using iso-surfaces of the λ_2-criterion coloured by static pressure in Fig. 2. Note, the results for $Re_D = 100$ are extruded in the spanwise direction for illustration purposes. It can be seen that, as expected, the near wake development is defined by the formation and evolution of the von Kármán rollers for all Reynolds numbers investigated. The dominant spanwise vortices undergo notable deformations associated with the formation of three-dimensional secondary structures for $Re_D \geq 300$. For $Re_D = 300$, a hyperbolic flow instability in the shear regions between primary vortex cores, termed "mode B" instability (Williamson 1996), leads to the development of secondary streamwise vortices which persist with a spanwise wavelength of $\lambda_z/D \approx 1.0$ (Williamson 1996; Scarano and Poelma 2009). For $Re_D = 1575$, turbulent transition occurs in the separated shear layers and precedes primary vortex formation. The wake consists of a plethora of secondary structures interacting with the primary spanwise rollers in a random fashion. As progressively finer scale structures develop with increasing Re_D, characteristic spatial and temporal scales in the wake pressure fields also decrease, as expected, which is the primary reason for selecting these three test cases for the present study.

2.2 Synthetic PIV and pressure estimation optimization

Synthetic PIV data were obtained by sampling planar $x - y$ velocity fields from the DNS solutions at $z = 0$ (midspan) on an equispaced Cartesian grid on the domain $-2D < x < 2D$ and $-2D < y < 2D$ for a range of f_{acq} and WS. Similar to the approach employed in previous studies (e.g., Charonko et al. 2010; Azijli and Dwight 2015), Gaussian random noise was added to the synthetic velocity fields proportional to the magnitude of each velocity component ($\tilde{u} = u(1 + \varepsilon_u)$) to simulate measurement noise. The noise level (ε_u) was varied between 0 and 2.5% in 0.25% increments to capture the initial error response characteristics, which for a given methodology have been shown to extrapolate to higher noise levels (de Kat and van Oudheusden 2012; Charonko et al. 2010). To estimate pressure from the synthetic data, Eulerian spatial and temporal derivatives of the velocity field were calculated with second-order central difference estimators (Eq. 5) and used to estimate the material acceleration and viscous terms in Eq. 3. The viscous terms in the Navier–Stokes equations were found to be non-negligible for $Re_D = 100$, and hence were included for all Re_D. A parametric study was performed to investigate the effects of Reynolds number (Re_D), spatial resolution (WS), temporal resolution (f_{acq}), velocity field noise level (ε_u), and pressure estimation method on the accuracy of instantaneous pressure field estimations (p). The investigated parameters are summarized in Table 2.

Four common pressure integration techniques were compared: (1) omni-directional line integration (Liu and Katz 2006), (2) eight-path integration (Dabiri et al. 2014), (3) Poisson equation (Gurka et al. 1999), and (4) local least squares iteration (Tronchin et al. 2015). For each temporal resolution (f_{acq}), spatial resolution (WS),

Table 2 List of pressure estimation methodologies employed in the current study and ranges of parameters investigated in the parametric study

Estimation methodology	Re_D	ε_u	D/WS	f_{acq}/f_S
Omni-directional				
Eight-path	100, 300, 1575	0–2.5%	5–100	7.8–1000
Poisson equation				
Local least squares				

and noise level (ε_u) investigated in the parametric study, instantaneous velocity fields were sampled at six different phases over half a vortex shedding cycle ($\theta = 0$, $\pi/6$, $\pi/3$, $\pi/2$, $2\pi/3$, $5\pi/6$) and five refreshed noise profiles were generated at each phase, resulting in a total of 30 unique velocity fields for each combination of parameters investigated, from which pressure is estimated using each integration technique. The error in each estimated pressure field (ε_p) was quantified using the spatial standard deviation of the difference between the estimated (p) and DNS (p_{ex}) pressure field (Eq. 8). For a given combination of parameters, the error response was then characterized by the mean ($\overline{\varepsilon}_p$) and standard deviation (σ_{ε_p}) of this error computed over the 30 pressure estimates.

$$\varepsilon_p = \frac{\sqrt{\sum (p - p_{ex})^2 / N}}{\frac{1}{2} \rho U_\infty^2} \tag{8}$$

The implementation of boundary conditions can have considerable effects on the accuracy of pressure estimates (Pan et al. 2016). For the iterative methods (omni-directional, eight-path, and local least squares), the boundary conditions were implemented following the approach employed in the studies that proposed these techniques (Liu and Katz 2006; Dabiri et al. 2014; Tronchin et al. 2015), namely, where the domain was initialized to zero pressure before integrating the pressure gradient over the inner domain and boundaries. Additionally, for the omni-directional and eight-path methods, the boundary pressures were initialized by a line integral of the pressure gradient field around the boundary, starting at $p_{1,1} = 0$ at the bottom left corner point. Based on initial convergence tests, a fixed number of pressure gradient integration iterations were performed. Specifically, the omni-directional and eight-path methods used 5 iterations, and the local least squares method used 3000 iterations. For the Poisson equation method, the Laplacian of the pressure field (Eq. 4) was discretized using a 5-point second-order central difference scheme and Neumann boundary conditions were imposed through the use of ghost grid points at the outlet and cylinder boundaries to complete the five point scheme where adjacent nodes lie outside the domain. The pressure values at the ghost points were evaluated using the pressure gradient from the Navier–Stokes equation and the nodal pressure on the opposing side of the five point scheme (e.g., $p_{i+1,j} = p_{i-1,j} + 2\Delta x \frac{\partial p}{\partial x}_{i,j}$). Neumann boundary conditions were implemented for the Poisson equation method on all boundaries and an additional constraint equation was added to the system to specify $p_{1,1} = 0$. The resulting system of equations is over-constrained and the solution is the least-squares solution (Trefethen 2000). For each method, the relative pressure field was solved for initially, and a constant value was then added to each field such that the Bernoulli equation extended to irrotational, inviscid, unsteady advective flow with small mean velocity gradients (Eq. 9) (de Kat and van Oudheusden 2012) was satisfied, on average, at the top and bottom boundaries.

$$p + \frac{1}{2}\rho(\overline{\mathbf{u}} \cdot \overline{\mathbf{u}} + \overline{\mathbf{u}' \cdot \mathbf{u}'}) = p_\infty + \frac{1}{2}\rho U_\infty^2 \tag{9}$$

The parametric study and analytic models developed in the current study use Eulerian estimates for the material acceleration (Eq. 5), since a comparison with a second order Lagrangian scheme for material acceleration estimation (Eqs. 6, 7) resulted in minor differences in error levels of the pressure evaluations for $25 \leq f_{acq}/f_S \leq 1000$ when three velocity fields at $t_0 - dt$, t_0, and $t_0 + dt$ were utilized for both methods. However, the extension of the analysis to Lagrangian material acceleration reconstructions over N fields is discussed using second order trajectory estimates (Eqs. 6, 7) between fields separated by $\pm M dt$, $\pm (M-1)dt, \ldots$, where $N = 2M + 1$, with the material acceleration estimated via a second order polynomial fit to the resulting trajectory (Lynch and Scarano 2014).

3 Results

The results of the parametric study yield a data set of about 110,000 pressure field cases. Using this data set, the pressure estimation techniques are compared across a range of spatial resolutions (WS), temporal resolutions (f_{acq}), and velocity noise levels (ε_u) in laminar, transitional, and turbulent flows.

3.1 Comparison of pressure estimation methodologies

It has been demonstrated in one-dimensional parametric studies (Charonko et al. 2010; Violato et al. 2011; de Kat and van Oudheusden 2012; Tronchin et al. 2015) that optimal temporal ($f_{acq,opt}$) and spatial (WS$_{opt}$) resolutions can be determined for a given flow such that the combined truncation (ε_{trunc}) and random (ε_{rand}) uncertainty propagation to the pressure field estimate is minimized. Since the optima may vary based on the pressure integration technique employed, it is necessary to estimate these parameters before a comparison between methods can be carried out. Figure 3 shows the variation of the mean pressure error response ($\overline{\varepsilon}_p$) with f_{acq} and WS, for each tested technique and Reynolds number, when the synthetic velocity fields are contaminated with 2.0% Gaussian white noise. The magnitude of the mean pressure error is also illustrated by
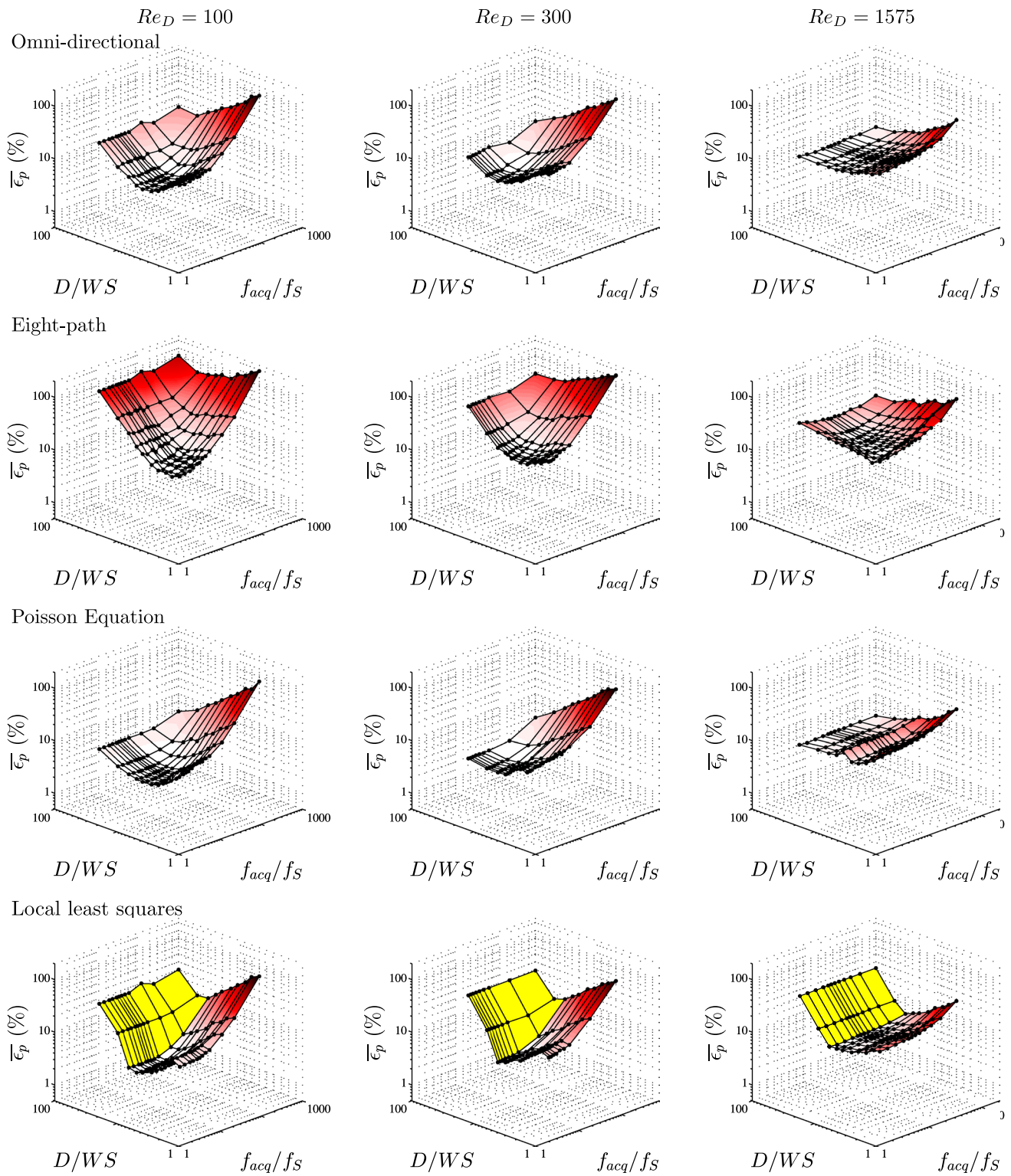
Fig. 3 Optimization surfaces showing the mean pressure field error ($\overline{\epsilon}_p$) for $\epsilon_u = 2\%$ for the ranges of spatial and temporal resolutions investigated for each Reynolds number and pressure estimation method investigated. Pressure estimations which are not converged are coloured in *yellow*

the white to red colormap on the surface, with the optimal sampling parameters identified either by the minima or the whitest region of each surface. The surface sections coloured yellow indicate where pressure estimation is uncoverged for the local least squares approach due to insufficient iteration of the solver to mitigate the directional propagation of error for the high spatial resolution calculations (D/WS ≥ 50). Note that optimal values cannot be strictly defined in every case due to the minima lying on the boundaries of the parametric study. For example, the optima for the eight-path method, for each Reynolds number investigated, likely lies beyond the minimum f_{acq}/f_S investigated, and the optima for the omni-directional method and Poisson equation for $Re_D = 1575$ is likely located beyond the maximum D/WS investigated. However, the curvature of the optimization surfaces at the boundaries suggest that the optimal values are located not far beyond the boundaries of the parametric study, and that the difference between the pressure error at the optimal point and the boundary point is comparable to the differences due to the resolution of the parametric study. The optimization surfaces exhibit similar topology for $Re_D = 100$, 300, and 1575 (left to right, respectively in Fig. 3), resembling sections of ellipsoid surfaces, and in most cases, local minima are present within the investigated range of parameters. For higher values of D/WS and f_{acq}/f_S, increasing these parameters causes the error to increase, approximately following a power law. On the other hand, decreasing D/WS and f_{acq}/f_S below the optimal values causes a more gradual increase in the pressure error. Notably, for increasing Reynolds number, the minimum error increases significantly, which is attributed to the increasing three-dimensional error (ε_{3D}) caused by neglecting the out of plane velocities and gradients. This causes changes in the random and truncation uncertainty propagation, resulting in changes in the temporal and spatial resolution leading to a less significant effect on the total pressure error. The values of optimal sampling parameters for $\varepsilon_u = 2\%$, identified in Fig. 3, are shown in Table 3. As expected, the optimal spatial resolutions (WS$_{opt}$) for each

method decrease with increasing Reynolds number as the spatial scales (λ_x) of the flow decrease. On the other hand, the optimal acquisition frequencies ($f_{acq,opt}/f_S$), when normalized by the shedding frequency, do not show a pronounced dependency on the Reynolds number within the uncertainty bounds. This is attributed primarily to two factors. First, the dominant vortical structures shed at f_S dominate the pressure fluctuations. Moreover, the main secondary structures that appear at higher Reynolds numbers are associated with time scales within an order of magnitude of $1/f_S$, and are adequately captured in estimated pressure fields acquired with $f_{acq}/f_S > 10$. Second, the error response surfaces in Fig. 3 flatten out near optimal acquisition frequencies making a precise determination of the optimal frequency challenging, which is the main reason for the relatively large uncertainty bounds for this quantity in Table 3. The development of practical guidelines for the selection of optimal sampling parameters will be discussed further in the next section.

To compare the accuracy of the methods at different velocity noise intensities, the mean ($\bar{\varepsilon}_p$) and standard deviation (σ_{ε_p}) of the pressure error response, extracted at WS$_{opt}$ and $f_{acq,opt}$ for each ε_u, are plotted in Fig. 4. It can be seen that the eight-path integration method exhibits consistently higher error sensitivity than the other methods, showing a comparable response for low ε_u but a significantly increased response in $\bar{\varepsilon}_p$ for more intense noise environments. Inspecting the corresponding pressure integration results (Fig. 5) indicates that the method suffers from high degrees of isotropic noise as the contour topology and pressure magnitudes are, on the average, close to the DNS reference (Fig. 5) but have a high degree of superimposed noise. The high noise sensitivity of the eight-path method is attributed to the lower number of line-integrals used, compared to the omni-directional method, which is a similar method that uses the average of significantly more line-integrals to calculate the fluid pressure at each point. The high noise sensitivity also causes the identified optimal sampling

Table 3 Optimal sampling parameters for $\varepsilon_u = 2\%$

| Pressure technique	$Re_D = 100$ D/WS$_{opt}$	$Re_D = 100$ $f_{acq,opt}/f_S$	$Re_D = 300$ D/WS$_{opt}$	$Re_D = 300$ $f_{acq,opt}/f_S$	$Re_D = 1575$ D/WS$_{opt}$	$Re_D = 1575$ $f_{acq,opt}/f_S$
Omni-directional	$20^{+5.0}_{-5.7}$	$25.3^{+6.3}_{-4.2}$	$33.3^{+16.7}_{-8.3}$	$20.4^{+2.6}_{-2.0}$	$100^{+50.0}_{-50.0}$	$15.6^{+20.8}_{-7.81}$
Eight-path	$6.7^{+1.6}_{-4.4}$	$12^{+3.8}_{-3.8}$	$14.3^{+5.7}_{-3.2}$	$20.4^{+2.6}_{-2.0}$	$20^{+5.0}_{-5.7}$	$21.7^{+14.6}_{-6.24}$
Poisson equation	$25^{+8.3}_{-5.0}$	$31.6^{+4.5}_{-6.3}$	$50^{+50.0}_{-16.7}$	$23.0^{+3.3}_{-2.6}$	$100^{+50.0}_{-50.0}$	$10.9^{+32.8}_{-3.1}$
Local least squares	$25^{+8.3}_{-5.0}$	$21.1^{+4.2}_{-5.3}$	$33.3^{+16.7}_{-8.3}$	$20.4^{+2.6}_{-2.0}$	$33.3^{+16.7}_{-8.3}$	$10.9^{+32.8}_{-3.1}$

Uncertainty bounds given by the local resolution of the parametric study at each optimum
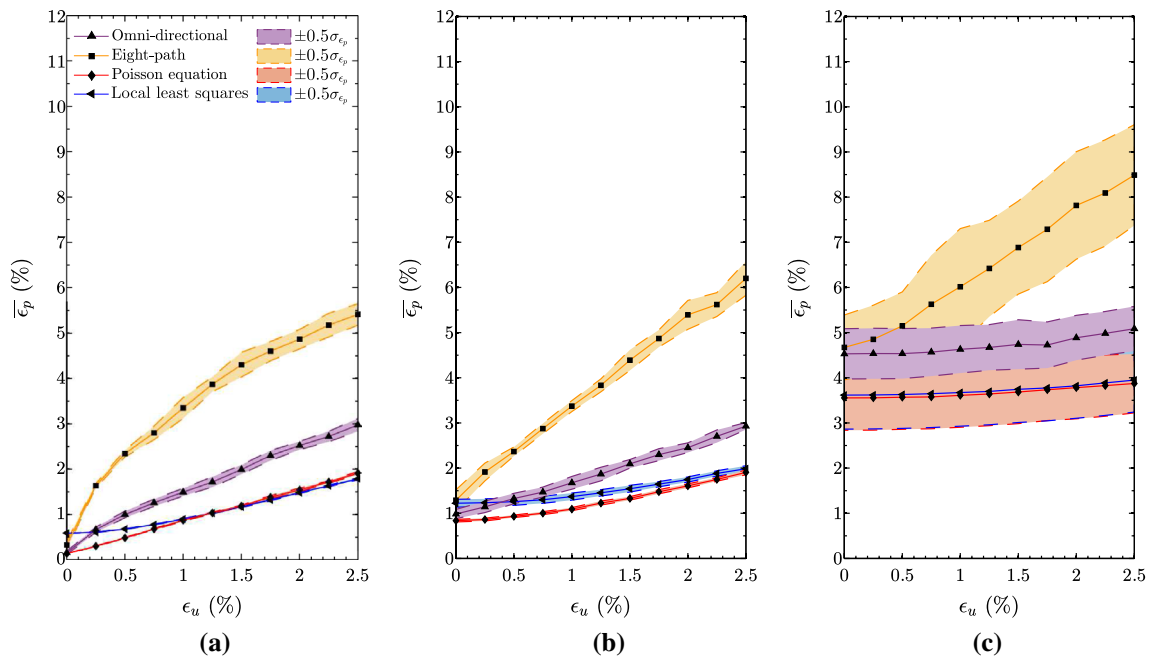
Fig. 4 Mean pressure field error (ε_p) versus velocity field error (ε_u) from each pressure integration method investigated for **a** $Re_D = 100$, **b** $Re_D = 300$, and **c** $Re_D = 1575$. *Filled regions* indicate one standard deviation of the pressure field error. For each ε_u, optimal WS_{opt} and $f_{acq,opt}$ were used for the pressure estimation
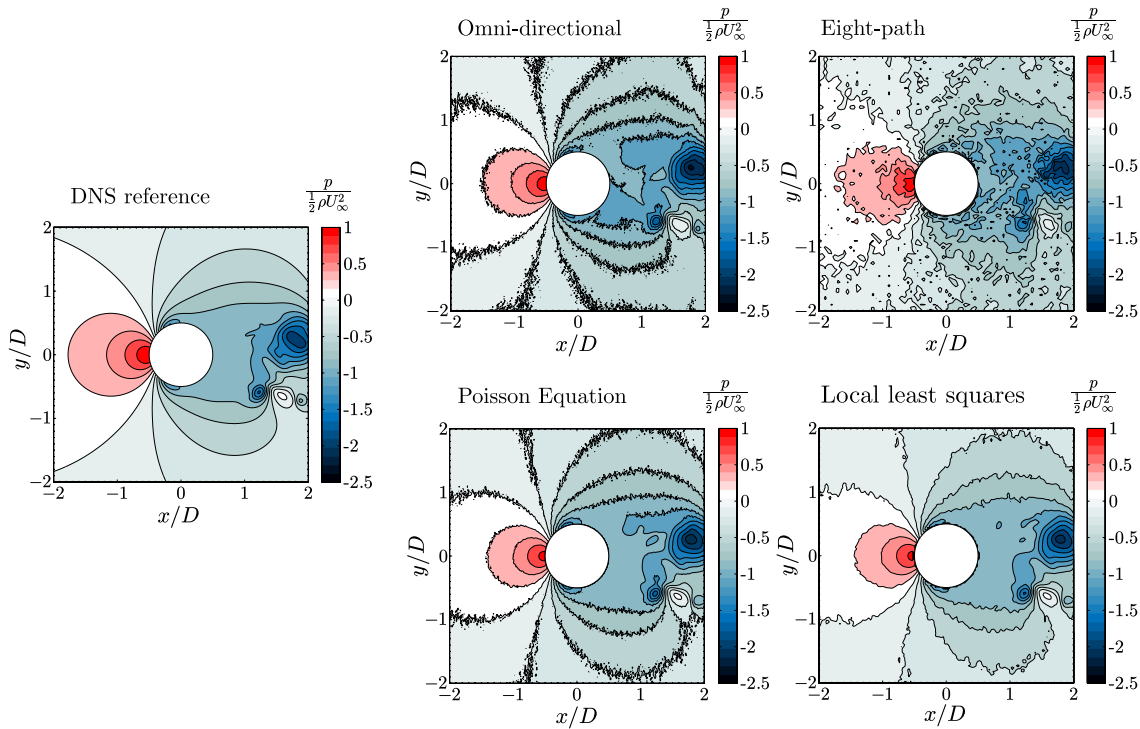
Fig. 5 Reference pressure from DNS data, along with pressure estimations at respective optimal D/WS_{opt} and $f_{acq,opt}/f_s$ for each method at $\varepsilon_u = 2\%$ and $Re_D = 1575$

parameters for the eight-path method to be shifted relative to the other three tested methods (Table 3). In contrast, the omni-directional, Poisson equation, and local least squares methods exhibit relatively low sensitivity to the velocity noise environment (ε_u), with maximum resulting error levels of 2–5% at $\varepsilon_u = 2.5\%$ depending on Re_D (Fig. 4a–c). In particular, for $Re_D = 1575$ (Fig. 4c), the pressure error response shows a change of less than 1% across the entire range of velocity noise intensities studied. This insensitivity is due to the relatively high base three-dimensional error present for $Re_D = 1575$ ($\varepsilon_{3D} \approx 4\%$), compared to the lower Reynolds numbers, caused by the two-dimensional assumptions imposed on the three-dimensional flow. This implies that, when significant inaccuracies in pressure estimation exist due to three-dimensional effects, contamination of the pressure gradient field by relatively small random errors in velocity measurements has a smaller additive effect on the pressure error response. The Poisson equation and local least squares method are the least sensitive to velocity fields noise, exhibiting the smallest change in $\overline{\varepsilon}_p$ over $\varepsilon_u = 0 - 2.5\%$. It should be noted that, since the errors in Fig. 4 are quantified by the standard deviation of the difference between the estimated pressure field and DNS solution (Eq. 8), they pertain to the relative pressure field ($p - p_\infty$). The error associated with establishing the absolute pressure through the application of the modified Bernoulli equation at the side boundaries was approximately 1% for all the pressure estimation methods investigated.

The accuracy of the surface pressure distribution ($C_p(\theta)$) estimation is of particular interest since it may be used to extract instantaneous structural loading (van Oudheusden et al. 2007). Figure 6 presents a comparison of the surface pressure estimations with the DNS reference for $Re_D = 100, 300$ and 1575. For each methodology, the pressure integrations were performed with a velocity noise level of $\varepsilon_u = 2\%$ and sampled at each method's WS_{opt} and $f_{acq,opt}$. The results indicate that the Poisson equation method estimates the surface pressures best across all the Reynolds numbers investigated, though the omni-directional and local least squares methods perform favourably as well. In comparison, surface pressure distributions resulting from the eight-path method have significant data scatter; however the scatter is approximately centred around the DNS pressure solution, so that its detrimental effect on structural loads is expected to be lower than the associated surface pressure errors. The utilization of the planar results for the extraction of surface pressure loading is deemed acceptable for all Reynolds numbers investigated, as the omni-directional, Poisson equation, and local least squares methods show remarkable agreement with the DNS solver pressures, even for relatively high $\varepsilon_u = 2\%$, as well as in turbulent shedding regimes (Fig. 6c). Despite average pressure field errors reaching approximately $\overline{\varepsilon}_p = 3-5\%$ for $\varepsilon_u = 2\%$ and $Re_D = 1575$ (Fig. 4c), the surface pressures rarely deviated from the DNS reference by more than 1%. The most significant pressure field errors are concentrated in the wake regions where flow three-dimensionalities and complex vortex development occur.

3.2 Pressure PIV uncertainty minimization

The results of the parametric study indicate the existence of optimal f_{acq} and WS_{opt} for various ε_u, Re_D, and pressure integration methodology which minimize the RMS pressure field error (Fig. 3; Table 3). It is of interest to develop a model that can be employed to estimate optimal
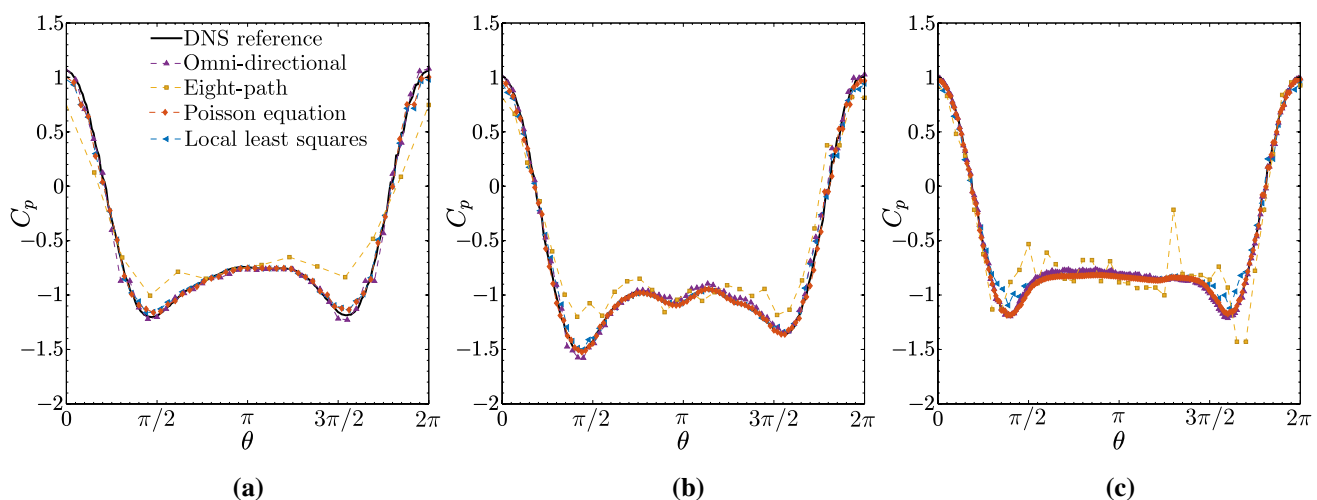
Fig. 6 Instantaneous surface pressure distributions from each method investigated, contaminated with $\varepsilon_u = 2\%$ velocity field error, for **a** $Re_D = 100$, **b** $Re_D = 300$, and **c** $Re_D = 1575$. $C_p(\theta)$ is nearest neighbour interpolated from the pressure evaluations sampled at identified optimal WS_{opt} and $f_{acq,opt}$

data acquisition parameters in experimental studies where pressure estimation is of interest. Such a model is developed here based on the following uncertainty propagation analysis.

Neglecting viscous terms, the uncertainty in the determination of the pressure gradient ($\varepsilon_{\nabla p}$, Eq. 10) can be expressed by the contributions of the propagation of the velocity error (ε_u, Eq. 11) (de Kat and van Oudheusden 2012) through the derivative estimators, and the truncation error terms arising from finite resolution of the derivative estimators (Etebari and Vlachos 2005) (ε_{trunc}, Eq. 12).

$$\varepsilon_{\nabla p}^2 \approx \rho \varepsilon_{Du/Dt}^2 \approx \rho \varepsilon_u^2 |u|^2 \left(\frac{f_{acq}^2}{2} + \frac{|u|^2}{2WS^2} + |\nabla u|^2 \right)$$
$$+ \frac{WS^4}{36}(\nabla^3 u)^2 |u|^2 + \frac{1}{36 f_{acq}^4} \left(\frac{\partial^3 u}{\partial t^3} \right)^2 \tag{10}$$

$$\varepsilon_{rand} = \rho \varepsilon_u |u| \sqrt{\frac{f_{acq}^2}{2} + \frac{|u|^2}{2WS^2} + |\nabla u|^2} \tag{11}$$

$$\varepsilon_{trunc} = \rho \sqrt{\frac{WS^4}{36}(\nabla^3 u)^2 |u|^2 + \frac{1}{36 f_{acq}^4} \left(\frac{\partial^3 u}{\partial t^3} \right)^2} \tag{12}$$

Equations 10–12 suggest minimizing the pressure gradient uncertainty requires balancing between the propagation of random error, which decreases for increasing WS and decreasing f_{acq}, and the truncation error, which decreases for decreasing WS and increasing f_{acq}. To model how the pressure gradient uncertainty propagates to pressure field uncertainty, a line-integration serves as a suitable approximation for the techniques employed in this study. In particular, at a single time-step, the omni-directional, eight-path, and local least squares methods rely on a sequential integration of ∇p over a finite number of WS to estimate p on the domain. Similarly, although the Poisson equation solves local equations simultaneously across the domain, the solution can nevertheless be cast as an integral of the pressure gradient field using Green's functions. Hence, assuming uncorrelated pressure gradient error, the resulting pressure field uncertainty (ε_p) relates to the pressure gradient uncertainty ($\varepsilon_{\nabla p}$) according to:

$$\varepsilon_p^2 = \sum^{\gamma/WS} \varepsilon_{\nabla p}^2 (WS)^2 \approx \gamma \varepsilon_{\nabla p}^2 WS \tag{13}$$

where γ is the characteristic length scale of a single line-integration (e.g., domain length). An optimization problem $\min\{\varepsilon_p^2 : f_{acq} > 0, WS > 0\}$ can now be solved for Eq. 13 with respect to f_{acq} and WS through a critical point analysis. The solution is given by Eqs. 14 and 15.

$$f_{acq,opt} = \left(\frac{(\partial^3 u/\partial t^3)^2}{9 \varepsilon_u^2 |u|^2} \right)^{1/6} \tag{14}$$

$$WS_{opt}^6 \frac{7(\nabla^3 u)^2 |u|^2}{36} + WS_{opt}^2 \left(\frac{3}{2}(\varepsilon_u f_{acq})^2 + 3\varepsilon_u^2 |\nabla u|^2 \right.$$
$$\left. + \frac{3}{36 f_{acq}^4} \frac{\partial^3 u^2}{\partial t^3} \right) + \varepsilon_u^2 |u|^2 / 2 = 0 \tag{15}$$

The result decouples the solution for the optimal temporal resolution (f_{acq}) from the dependence on the spatial resolution (Eq. 14). However, the solution for the optimal spatial resolution retains temporal terms (Eq. 15). This is due to the coupling caused by the propagation of $\varepsilon_{\nabla p}$ through the line-integrations which is $\propto \varepsilon_{\nabla p} WS$, resulting in a 6th order polynomial for WS_{opt}. For planning experiments, the solution remain intractable a priori due to its dependence on unknown velocity gradients. However, temporal and spatial derivatives of the flow may be approximated assuming the characteristic velocity (U_∞) varies periodically (i.e., sinusoidally) with the time scales ($1/f_{flow}$) and selecting appropriate spatial scales (λ_x) for a given vortex dominated flow. Substituting these approximations into Eqs. 14 and 15 simplifies them to:

$$f_{acq,opt} \approx \frac{2\pi f_{flow}}{(3\varepsilon_u)^{1/3}} \tag{16}$$

$$\frac{7}{18\varepsilon_u^2} \left(\frac{2\pi WS_{opt}}{\lambda_x} \right)^6 + 6 \left(\frac{2\pi WS_{opt}}{\lambda_x} \right)^2 + 1 = 0 \tag{17}$$

Inspection of Eq. 17 reveals that, for $\varepsilon_u = 0–3\%$ typically found in PIV experimentation, the leading, 6th order term dominates and the 2nd order term in the polynomial is negligible. Hence the model for the optimal spatial resolution can be simplified further to:

$$WS_{opt} \approx \left(\frac{18\varepsilon_u^2}{7} \right)^{1/6} \frac{\lambda_x}{2\pi} \tag{18}$$

where WS_{opt} is independent of f_{acq} for small ε_u. This can also be inferred from the optimization surfaces presented in Fig. 3, which conform to, on the average, ellipsoid sections with major and minor axes aligned with the temporal and spatial axes. This result implies that the optimal temporal and spatial resolutions obtained from one-dimensional parametric studies in Charonko et al. (2010) and Violato et al. (2011) are valid as absolute optimums for the respective intensity of the noise environment, and may be compared to the data in the present study. It is important to note that the derivation of Eqs. 16 and 18 is insensitive to reformulating

Eq. 13 as an average of multiple line integrations or incorporating terms representing the boundary error at the start of each line integration. The presented formulation also assumes uncorrelated velocity field error, which will not be the case if interrogation windows are overlapped during PIV processing (Sciacchitano and Wieneke 2016), and does not account for the spatial filtering implicit in the use of finite interrogation windows in PIV processing. However, it was verified that adding correlated velocity field errors after smoothing the velocity field with a 3×3 kernel had minimal effect on the results pertaining to the locations of the optimal sampling parameters and comparison of methods presented in Figs. 4, 5 and 6.

To validate the derived model (Eqs. 16, 18), it is applied to the flow cases considered in the current study. For circular cylinders in cross-flow, the characteristic frequency scale (f_{flow}) is approximated as the frequency of vortex shedding $f_S = St_D D/U_\infty$ and the characteristic spatial wavelength (λ_x) is approximated as twice the shear layer thickness, approximated according to $\delta_{sl} = 7.5D/Re_D^{1/2}$ (Williamson 1996; Roshko 1993). The optimal temporal and spatial resolutions for pressure evaluation in flow over a circular cylinder may now be calculated using Eqs. 16 and 18, respectively. It can be seen from Eqs. 16 and 18 that a universal scaling for the $f_{acq,opt}$, and WS_{opt} is achieved in the form $f_S/f_{aqc,opt}$ and λ_x/WS_{opt}. The results from the present study cast in this form are presented in
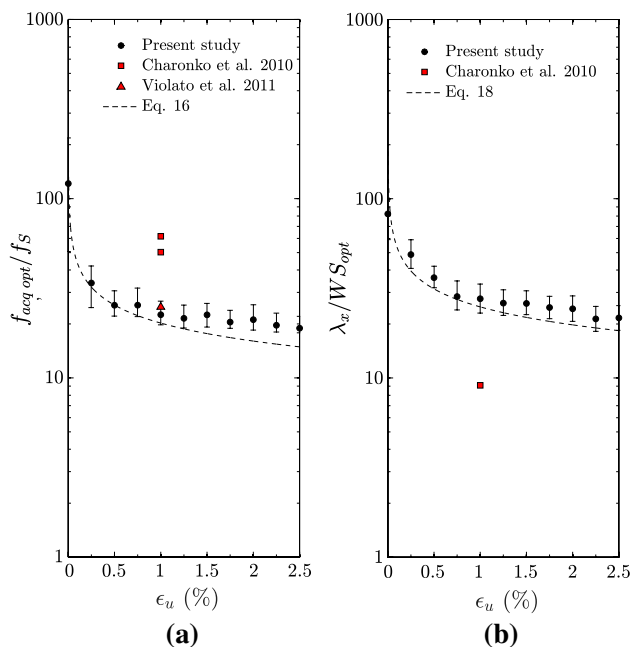
Fig. 7a, b, along with relevant data found in the literature for a decaying vortex (Charonko et al. 2010), pulsitile flow (Charonko et al. 2010), and a rod airfoil (Violato et al. 2011). The present data show good collapse, and the model shows close agreement with the parametric data as well as optima reported in other investigations on different flow topologies. Based on the results, a general recommendation can be made for a range of optimal data acquisitions parameters as $f_{acq}/f_{flow} = 18$–30 and $\lambda_x/WS = 14.3$–25 for the range of velocity error levels expected in a typical PIV experiment when Eulerian material acceleration estimation methods are applied. These results are in agreement with the resolution limitations suggested by de Kat and van Oudheusden (2012) of $\lambda_x/WS > 5$ and $f_{acq}/f_{flow} > 10$, who were primarily concerned with the effects on pressure peak response in the resulting fields. The current results suggest that utilizing resolutions up to twice the minimum limits on the acquisition frequency and four times the minimum limits on the spatial resolution recommended by de Kat and van Oudheusden (2012) will result in optimal performance, minimizing the spatial filtering effects caused by inadequate spatial or temporal resolutions without oversampling to an extent that random error effects become significant.

Figure 8a–d elucidate the relation between the data acquisition parameters and the pressure uncertainty predicted by Eq. 13. The identified minima, which stem from Eqs. 16 and 18, for λ_x/WS and f_{acq}/f_S, respectively, can be seen to be independent of the the Reynolds number. The pressure uncertainty remains within 1% of the minimum uncertainty for a relatively wide range of acquisition frequencies from $3 \leq f_{acq}/f_s \leq 200$ (Fig. 8a). In contrast, the requirements on the spatial resolution to remain within the same range of the minimum uncertainty are more stringent, namely $\lambda_x/WS = 14.3$–33.3 (Fig. 8c). Figure 8b, d decompose the total pressure uncertainty from Eq. 13 for $Re_D = 1575$ into contributions from truncation (ε_{trunc}) and random (ε_{rand}) error components. The results illustrate the regions where spatial or temporal resolutions become too fine, and propagation of random error dominates, and where they become too coarse and the truncation error term dominates. Comparing the current formulation to the bounds on the spatial and temporal resolution recommended by de Kat and van Oudheusden (2012), indicated by a dash-dotted line in Fig. 8b, d, it can be seen that the recommended spatial resolution bound corresponds to a region where the truncation error dominates, while the temporal resolution bound corresponds to a region with still acceptable uncertainty levels, beyond which truncation error begins to dominate.

It is important to note that when data is over-sampled temporally (i.e., $f_{acq} > f_{acq,opt}$), Lagrangian trajectory reconstructions over multiple velocity fields (e.g., Lynch and Scarano 2014) can be employed for more accurate
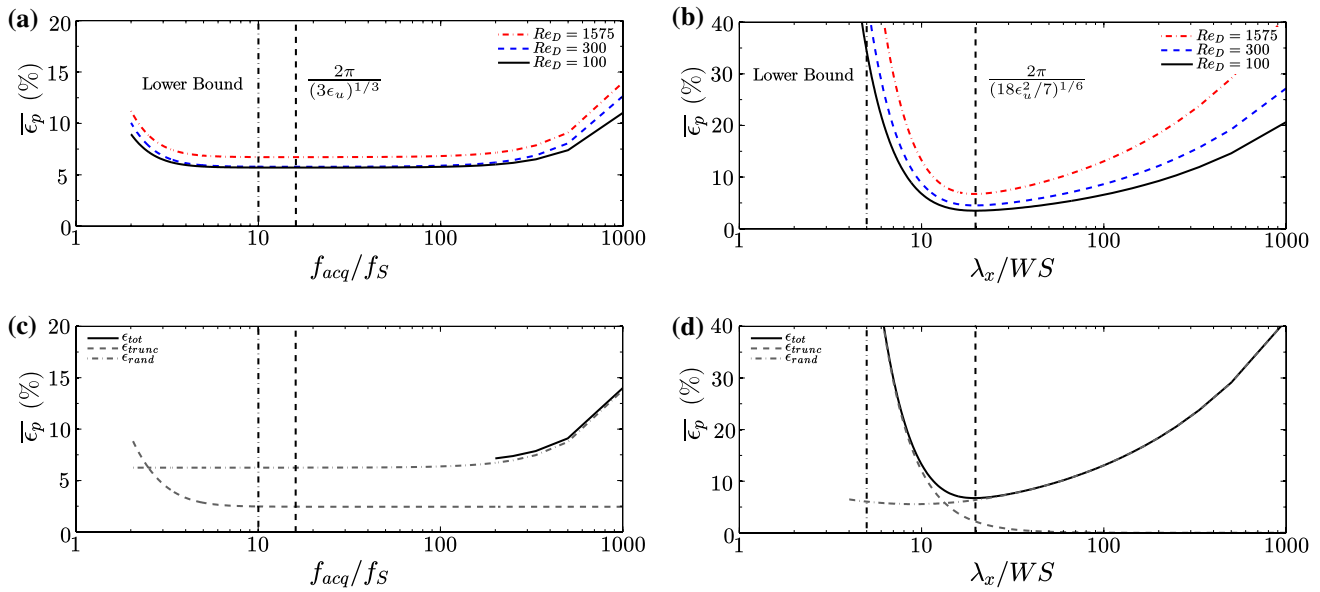

Fig. 7 a Optimal temporal resolutions $f_{acq,opt}$ normalized by the shedding frequency f_s amalgamated from all Reynolds numbers and methodologies tested and compared to available optimal data from other studies and **b** optimal spatial resolution WS_{opt} normalized by the spatial wavelength λ_x of the flow

Fig. 8 Pressure field uncertainty predicted from Eq. 13 with $\varepsilon_u = 2\%$ exhibiting Reynolds number similarity across (**a**) temporal resolution at fixed D/WS = 100 and **b** spatial resolution at fixed $f_{acq}/f_s = 50$ compared to bounds proposed by (de Kat and van Oudheusden 2012).
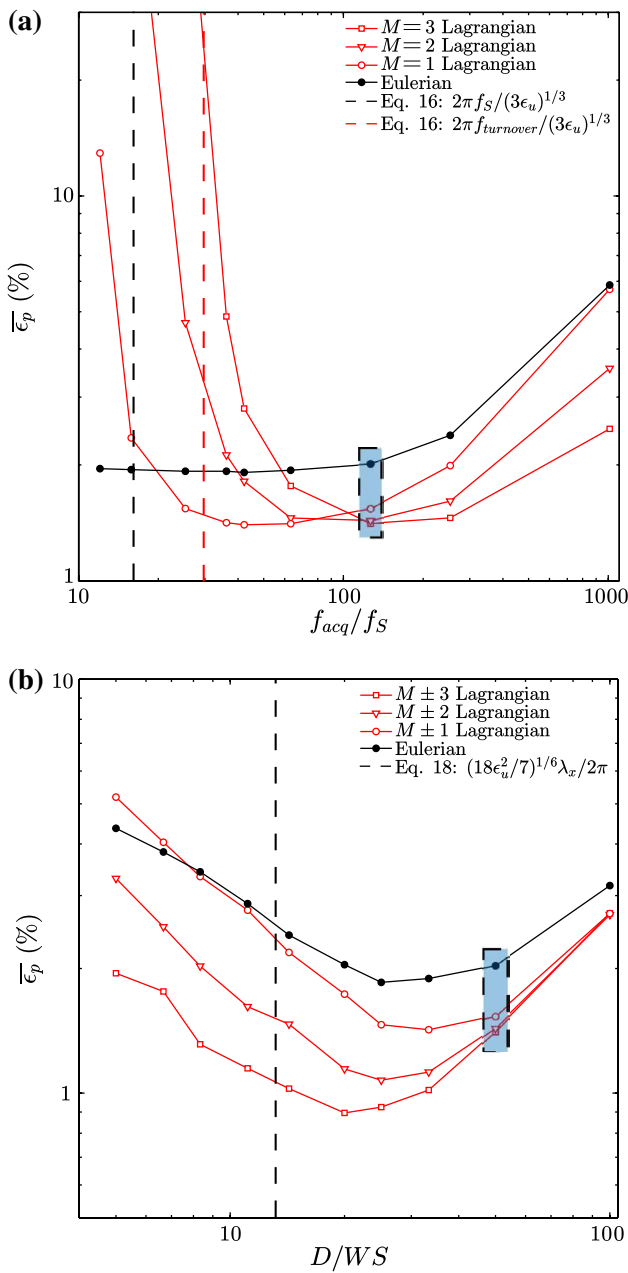
The uncertainty is decomposed into random and truncation components according to Eq. 13 using f_S and λ_x estimates, and the variation with **c** spatial and **d** temporal resolutions for $Re_D = 1575$ is shown

estimation of pressure, as low order trajectory reconstructions over longer kernels mitigates random error propagation. Figure 9 illustrates how average error levels change with respect to temporal and spatial resolution for the Eulerian methods used for the parametric study compared to Lagrangian material acceleration estimates over multiple velocity fields. For the Lagrangian estimates, the fluid trajectories are computed iteratively using a second order trajectory reconstruction (Eqs. 6, 7) at times $t_0 - Mdt$, $t_0 - (M-1)dt, \ldots, t_0, \ldots t_0 + (M-1)dt, t_0 + Mdt$, employing a second order polynomial fit function following the method by Lynch and Scarano (2014). The results show that the use of Lagrangian techniques for material acceleration estimation changes substantially the shapes of the optimization curves with respect to temporal resolution (Fig. 9a), while the changes for the spatial resolution (Fig. 9b) are less significant. For the temporal resolution, using the vortex turn over time ($f_{turnover} = U_\infty/\pi D$) (de Kat and van Oudheusden 2012) gives a reasonable estimate of the optimal acquisition frequency for the Lagrangian method with $M = 1$. However, as the kernel for material acceleration estimation is increased to $M = 2$ and $M = 3$, the optimum acquisition frequency increases proportionally, with $f_{acq,opt}/f_S \approx 50$ for $M = 1$, $f_{acq,opt}/f_S \approx 100$ for $M = 2$, and $f_{acq,opt}/f_S \approx 150$ for $M = 3$. This implies that when Lagrangian material acceleration estimates are employed for pressure estimation, velocity acquisition at $Mf_{acq,opt}$ is recommended, where $f_{acq,opt}$ is predicted from Eq. 16. If the data is under-sampled relative to the predicted optimum

($f_{acq} < f_{acq,opt}$), a significant increase in error levels can be observed for the Lagrangian estimates. If such a sub-optimal condition is dictated by limitations of the experiment, one may employ pressure estimation techniques which attempt to operate on temporally sparse data, such as VIC codes (Schneiders et al. 2016) or Taylor Hypothesis substitutions (de Kat et al. 2013; Laskari et al. 2016). In contrast to the temporal resolution results (Fig. 9a), the shape of the optimization curves for the spatial resolution (Fig. 9b) does not change significantly when different Lagrangian evaluations are employed, with the optimum shifting to coarser spatial resolutions as the kernel size for material acceleration estimation is increased.

3.3 Effect of three-dimensional flow structures

Besides the truncation and random error propagation varying with Re_D due to associated changes in the spatial and temporal scales of the flow, the onset of three-dimensional flow structures in transitional and turbulent wake regimes (Williamson 1989; Bloor 1964) will lead to addition errors (ε_{3D}) due to two-dimensional flow assumptions used for pressure estimation. For two-component, planar PIV, estimation of the pressure gradient from the two-dimensional Navier–Stokes equations neglects out-of-plane velocities and gradients. However, the onset of secondary instabilities in transitional flow regimes (Williamson 1989) (Fig. 2b) and turbulent regimes (Bloor 1964) (Fig. 2c) is associated

(a)

Legend:
- $M = 3$ Lagrangian
- $M = 2$ Lagrangian
- $M = 1$ Lagrangian
- Eulerian
- Eq. 16: $2\pi f_S/(3\epsilon_u)^{1/3}$
- Eq. 16: $2\pi f_{turnover}/(3\epsilon_u)^{1/3}$

y-axis: $\overline{\epsilon_p}$ (%)
x-axis: f_{acq}/f_S

(b)

Legend:
- $M \pm 3$ Lagrangian
- $M \pm 2$ Lagrangian
- $M \pm 1$ Lagrangian
- Eulerian
- Eq. 18: $(18\epsilon_u^2/7)^{1/6}\lambda_x/2\pi$

y-axis: $\overline{\epsilon_p}$ (%)
x-axis: D/WS

Fig. 9 Comparison of pressure estimation error using Eulerian and Lagrangian material acceleration estimates reconstructed over 3 ($M = 1$), 5 ($M = 2$), and 7 ($M = 3$) velocity fields using the Poisson equation for $Re = 100$ and $\epsilon_u = 2\%$ for **a** varying acquisition frequency with a constant spatial resolution $D/WS = 50$, and **b** varying spatial resolution with a constant acquisition frequency $f_{acq}/f_S = 123$. The common points where the one-dimensional parametric studies intersect are highlighted in *blue*

with three-dimensional vortex development, bound to result in errors in planar pressure estimations.

To evaluate the error in the pressure field caused by the presence of three-dimensional structures and decouple it from $\epsilon_{trunc}$, a comparison is carried out between pressure estimations obtained from 2D planar and 3D volumetric velocity data using the Poisson equation method for pressure estimation. The 3D volumetric velocity data are sampled from DNS at three equispaced $x-y$ planes with the spatial resolution in the spanwise direction (z) matching that in the $x-y$ plane. The difference between the integration from the planar data and the integration from the volumetric data serves as a measure of the three-dimensional error ($\epsilon_{3D} = |p_{3D} - p_{2D}|$). For studies employing planar measurements, it is also of interest to estimate the uncertainty in the pressure estimates caused by neglecting terms containing out of plane velocity and gradients. The x and y momentum equations from which the pressure gradient field is estimated are shown in Eqs. 1 and 2, including the three-dimensional terms. The additional terms are $w\frac{\partial u}{\partial z}$ and $w\frac{\partial v}{\partial z}$ for the x and y pressure gradients, respectively. When two-component, planar velocity measurements are performed, both the out of plane velocity and gradients in these terms are unknowns. However, in a developed turbulent wake, the spanwise gradients of each velocity component are similar in magnitude ($\frac{\partial w}{\partial z} \approx \frac{\partial v}{\partial z} \approx \frac{\partial u}{\partial z}$), since spanwise gradients in the flow are induced by randomly oriented vortex structures. This implies that the three-dimensional terms can be approximately related to the magnitude of $\frac{\partial w}{\partial z}$, which can be estimated by applying the continuity equation to the planar measurements in incompressible flow as $\frac{\partial w}{\partial z} = \frac{\partial u}{\partial x} + \frac{\partial v}{\partial y}$. Since the out of plane velocity w is expected to act as a pseudo-random variable in a spanwise homogeneous flow, a correlation between the magnitude of $w\frac{\partial u}{\partial z}$ or $w\frac{\partial v}{\partial z}$ (i.e., the neglected three-dimensional terms in Eqs. 1 and 2) and the planar divergence should be possible.

Figure 10a–c plot the instantaneous three-dimensional pressure field error ($\epsilon_{3D} = |p_{3D} - p_{2D}|$) based on a comparison between planar and volumetric pressure estimations for $Re_D = 100$, 300, and 1575, respectively, and Fig. 10d–f plot the corresponding planar divergence of the velocity field. The figures show that the three-dimensional pressure estimation errors develop locally with some minor propagation to neighbouring regions, and the regions of elevated pressure errors correlate with regions of higher planar divergence. Figure 11 presents the two-dimensional correlation maps of the standard deviation of the planar divergence field and the standard deviation of the three-dimensional error field for $Re_D = 300$, and $Re_D = 1575$. In both cases, the maximal peak is at zero spatial shift, indicating that the regions of three-dimensional error and planar divergence are well correlated. The correlation maps experience rapid drop off from zero spatial shift, indicating that quantities are strongly correlated in space. The exception is negative streamwise shifts, that exhibit slow drop off due to the error
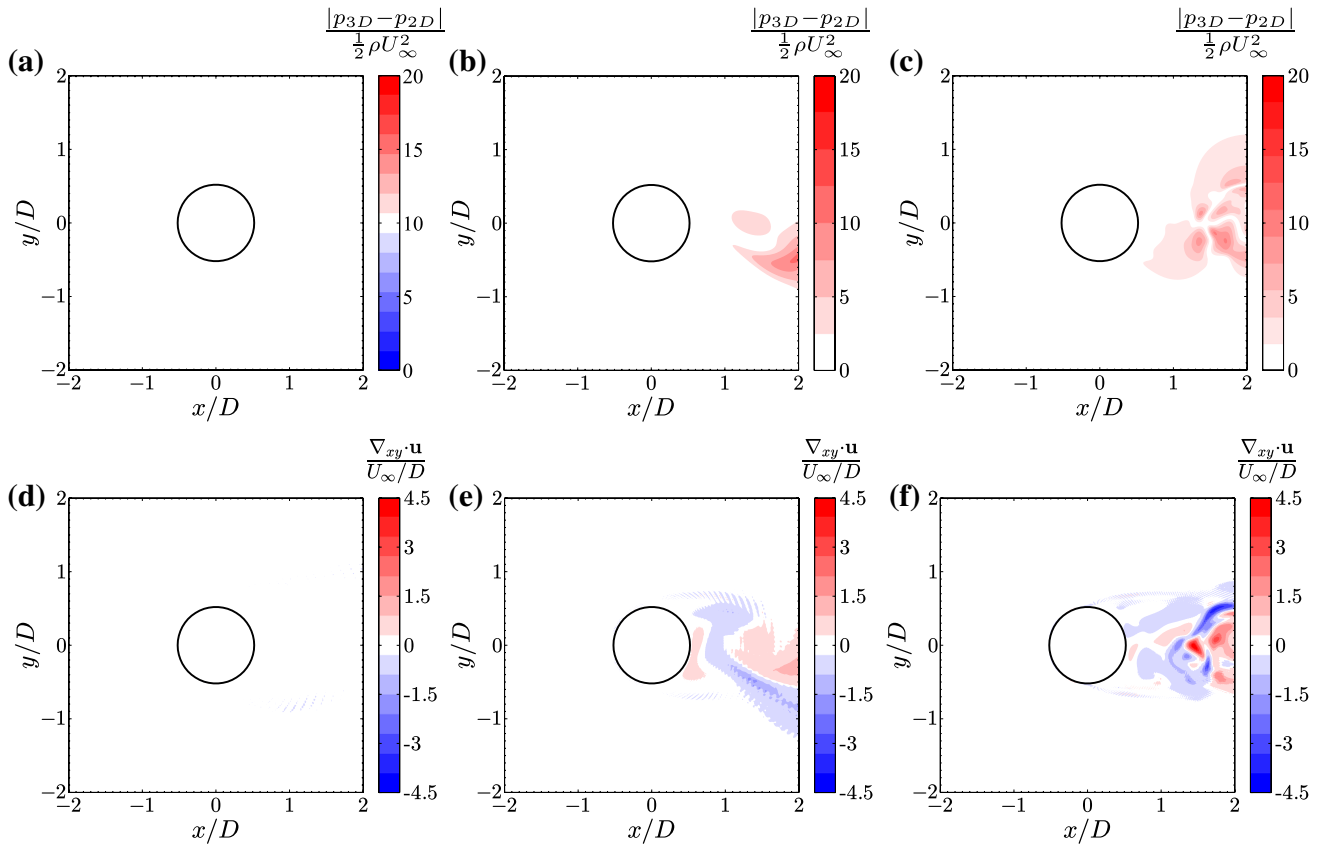
Fig. 10 Instantaneous planar divergence for **a** $Re_D = 100$, **b** $Re_D = 300$, and **c** $Re_D = 1575$. Instantaneous pressure field error for **d** $Re_D = 100$, **e** $Re_D = 300$, and **f** $Re_D = 1575$. Velocity data sampled at $D/WS = 100$ and $f_{acq}/f_s = 63 - 73$ and pressure field estimated using the Poisson equation method
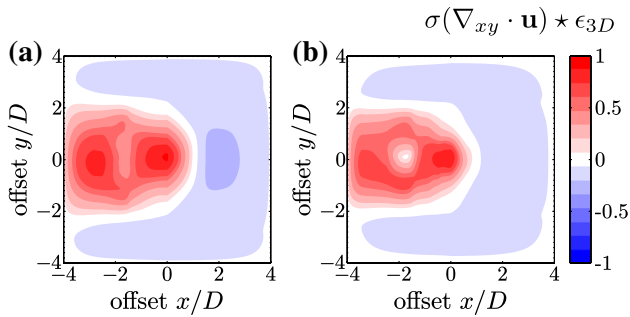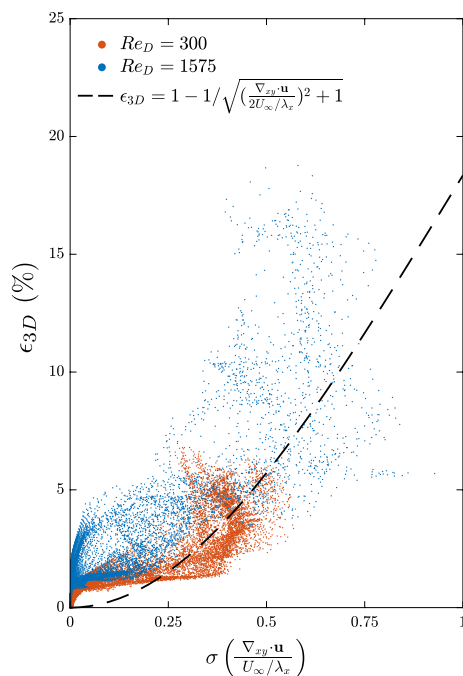

Fig. 11 Correlation maps of the standard deviation of the planar divergences with the three-dimensional pressure error for **a** $Re_D = 300$, and **b** $Re_D = 1575$

and divergence concentrating in the wake region which extends in the streamwise direction.

Figure 12 presents the variation in the standard deviation of the planar divergence in the wake with the three-dimensional error caused by the planar assumptions. A fit is provided, and can be used to estimate local uncertainty of the pressure estimations caused by utilizing planar data
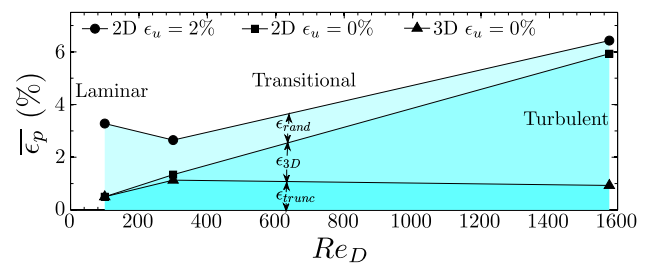
in a three-dimensional flow, by calculating the local planar divergence of the velocity data. The form of the fit is based on a three-dimensional trigonometric relation between the out of plane gradient ($\nabla_{xy} \cdot \mathbf{u}$) and characteristic values for the in plane gradients (U_∞/λ_x). Figure 12a shows a significant increase in characteristic planar divergence magnitudes from $Re_D = 300$ to $Re_D = 1575$, which directly results in a significant increase in the three-dimensional error in the wake. The increased three-dimensionality for $Re_D = 1575$ (Figs. 2c, 10c, f) is associated with stronger secondary vortex formation at finer scales compared to $Re_D = 300$. Localized pressure errors can exceed 20% of the dynamic pressure when using planar evaluation techniques (Fig. 10c). In contrast, local errors in pressure estimates from volumetric velocity data are within 1.2% of the DNS solution (not shown for brevity). For $Re_D = 300$, in a transitional regime, the induced three-dimensional flow of the mode B instability vortices is substantially weaker than that found for fully turbulent Reynolds numbers, and the three-dimensional errors are less pronounced (<15%). These results can be compared to those of Charonko et al. (2010), who found that three-dimensional errors using

Fig. 12 RMS of the three-dimensional error related to the standard deviation of the planar divergence of the velocity field

Fig. 13 Decomposition of the pressure field error into random, truncation, and three-dimensional components. Based on pressure evaluation using the omni-directional integration technique at $D/WS = 20$ and $f_{acq}/f_s = 63$–73. ε_{trunc} is the error using 3D NS equations for $\varepsilon_u = 0\%$, ε_{3D} is the difference between the errors using the 2D NS and 3D NS equations for $\varepsilon_u = 0\%$, and ε_{rand} is the additional error when using the 2D NS equations for $\varepsilon_u = 2\%$

planar techniques did not grow to significant levels until the measurement plane was misaligned over 30° from the planar velocity field (i.e., when the out-of-plane velocity gradients reaches 50% of the $x - y$ local values (Charonko et al. 2010). Similarly in the present results, pressure errors become significant (>5%) when the normalized divergence is greater than 0.5 (i.e., 50% of typical planar gradient values associated with the global vortex shedding).

To compare the relative magnitude of the three-dimensional errors to other errors affecting pressure estimation, Fig. 13 plots the base truncation error, three-dimensional error, and random error variation with Reynolds numbers spanning laminar ($Re_D = 100$), transitional ($Re_D = 300$) and turbulent ($Re_D = 1575$) regimes. The errors were decomposed based on evaluations of the pressure field using the omni-directional method at a fixed spatial and temporal resolution. Successive pressure fields were estimated for each Re_D using two-dimensional and three-dimensional calculations of the pressure gradient with and without velocity noise applied ($\varepsilon_u = 0\%$ or 2%). For $Re_D = 100$, the near wake development is essentially two-dimensional and the pressure error is due primarily to ε_u and ε_{trunc}, i.e., due to random error propagation and truncation error from the finite sampling resolution. For $Re_D = 300$, ε_{3D} becomes comparable to the other two errors due to the onset of mode B instabilities. For $Re_D = 1575$, ε_{3D} is dominant over the ε_{truc} and ε_{rand}. The truncation error shows little change for $Re_D = 300$–1575,

while the random error decreases for increasing Re_D. The substantial decrease in the random error contribution to the total pressure error for increasing Re_D is attributed to the growth of ε_{3D} with Re_D, which acts in a quasi-random manner in the wake, since the out-of-plane velocities and gradients are produced by passing turbulent structures of varying orientations. The addition of $\varepsilon_u = 2\%$ artificial random error onto the three-dimensional errors, which can reach over 20% locally (Fig. 10c), has a marginal additive effect on the total integrated pressure errors in the wake. This decreased sensitivity to random error is also seen in the optimization surfaces for $Re_D = 1575$ in Fig. 3 with respect to WS and f_{acq}. Hence, for turbulent regimes, the use of planar data for pressure reconstruction is shown to lead to significant errors where three-dimensional vortices develop. To resolve the pressure in a developed turbulent wake region with error levels below 5%, volumetric velocity data is required. However, planar techniques retain reasonable accuracy for estimating the surface pressures, since the magnitude of ε_{3D} near the cylinder surface is relatively low when transition occurs in the near wake (Figs. 6, 10). This conclusion is further supported by the experimental results of de Kat and van Oudheusden (2012), who find good agreement in their surface pressure transducer measurements with pressure measurements obtained from planar pressure PIV on the side of a square cylinder, where flow is predominantly two-dimensional. On the other hand, as pointed out by Ghaemi et al. (2012), volumetric data is required for accurate pressure reconstruction in a fully developed turbulent boundary layer.

4 Conclusion

Direct numerical simulations of flow over a circular cylinder in laminar, transitional and turbulent vortex shedding regimes are utilized to evaluate various pressure estimation

techniques typically applied to PIV measurements. The simulation data are uniformly sampled in time and space to mimic experimental PIV data, and a number of common methods are evaluated based on their ability to accurately estimate the wake and surface pressures when the mimicked PIV data is subjected to artificial, uncorrelated noise levels typical of experimentation (ε_u). The results indicate that the Poisson equation, omni-directional, and local least squares methods exhibit characteristically lower error sensitivity compared to the eight-path method. Hence, the Poisson equation, omni-directional, and local least squares methods are recommended for use in instantaneous pressure and force evaluation for immersed cylindrical bodies or similar vortex dominated shear flows.

An analytical model for the uncertainty associated with Eulerian pressure estimation from PIV data is developed and is shown to adequately predict the optimal spatial and temporal resolutions to minimize the pressure field uncertainty for a given flow with a given characteristic spatial wavelength (λ_x) and temporal scale (f_{flow}), as well as trends in these optimums with Re_D and ε_u. The model indicates ranges of temporal and spatial resolutions where the random error propagation or the truncation error is amplified significantly. The current study suggests $\lambda_x/WS = 14.3\text{–}25$ and $f_{acq}/f_{flow} = 18\text{–}30$ for optimal pressure integration, incorporating both the effect of random and truncation error on the resulting fields. For pressure estimations based on material acceleration estimates from Lagrangian trajectory reconstructions over multiple velocity fields, the optimal acquisition frequency increases proportional to the size of the velocity field kernel. The model is validated with a parametric study which computes pressure integrations over a range of spatial and temporal resolutions, velocity error levels, and Reynolds numbers. The resulting minima within the optimization set are extracted and show good agreement with the derived model. The equations for the optimal sampling parameters can be used, in conjunction with estimates of the dominant temporal and spatial scales of the flow, for the selection of experimental sampling parameters to minimize pressure estimation error.

Errors due to three-dimensional vortex structures are evaluated systematically via a comparison of pressure estimations obtained from two-dimensional, planar and three-dimensional, volumetric data. The results show that the increase in flow three-dimensionality moving from transitional ($Re_D = 300$) to turbulent ($Re_D = 1575$) shedding regimes leads to substantial local errors ($>20\%$) in the pressure fields estimated from planar measurements. These errors are reduced substantially (to $\approx 1\%$) when volumetric data is used, and hence volumetric measurements are essential for accurate evaluation of pressures in highly turbulent regions, i.e., in the turbulent wake away from the cylinder surface. On the other hand, when transition occurs in the near wake, surface pressure estimations from planar velocity fields can yield reliable results. Based on the analysis of the planar velocity divergence and three-dimensional error statistics, planar pressure techniques can be expected to produce reliable estimates in regions where the out-of-plane gradients are approximately less than half of in-plane velocity gradients.

References

Auteri F, Carini M, Zagaglia D, Montagnani D, Gibertini G, Merz CB, Zanotti A (2015) A novel approach for reconstructing pressure from PIV velocity measurements. Exp Fluids 56:45

Azijli I, Dwight R (2015) Solenoidal filtering of volumetric velocity measurements using Gaussian process regression. Exp Fluids 56:198

Azijli I, Sciacchitano A, Ragni D, Palha A, Dwight R (2016) A posteriori uncertainty quantification of PIV-based pressure data. Exp Fluids 57:72

Baur T, Köngeter J (1999) Piv with high temporal resolution for the determination of local pressure reductions from coherent turbulent phenomena. In: 3rd Int. Workshop on particle image velocimetry, Santa Barbara, pp 101–106

Blinde P, Michaelis D, van Oudheusden B, Weiss P, de Kat R, Laskari A, Jeon Y, David L, Schanz D, Huhn F, Gesemann S, Novara M, McPhaden C, Neeteson N, Rival D, Schneiders J, Schrijer F (2016) Comparative assessment of piv-based pressure evaluation techniques applied to a transonic base flow. In: 18th International symposium on the application of laser and imaging techniques to fluid mechanics, Lisbon, Portugal

Bloor M (1964) The transition to turbulence in the wake of a circular cylinder. J Fluid Mech 19:290–304

Charonko J, King C, Smith B, Vlachos P (2010) Assessment of pressure field calculations from particle image velocimetry measurements. Meas Sci Technol 21:105401

Dabiri J, Bose S, Gemmell B, Colin S, Costello J (2014) An algorithm to estimate unsteady and quasi-steady pressure fields from velocity field measurements. J Exp Biol 217:331–336

de Kat R, Ganapathisubramani B (2013) Pressure from particle image velocimetry for convective flows: a Taylors hypothesis approach. Meas Sci Technol 24:024002

de Kat R, van Oudheusden B (2012) Instantaneous planar pressure determination from PIV in turbulent flow. Exp Fluids 52:1089–1106

Elsinga G, Scarano F, van Oudheusden B (2006) Tomographic particle image velocimetry. Exp Fluids 41:933–947

Etebari A, Vlachos P (2005) Improvements on the accuracy of derivative estimation from DPIV velocity measurements. Exp Fluids 39:1040–1050

Fujisawa N, Tanahashi S, Srinivas K (2005) Evaluation of pressure field and fluid forces on a circular cylinder with and without rotational oscillation using velocity data from PIV measurement. Meas Sci Technol 16:989–996

Ghaemi S, Ragni D, Scarano F (2012) PIV-based pressure fluctuations in the turbulent boundary layer. Exp Fluids 53:1823–1840

Gurka R, Liberzon A, Hefetz D, Rubinstein D, Shavit U (1999) Computation of pressure distribution using PIV velocity data. In: 3rd

Int. workshop on particle image velocimetry, Santa Barbara, pp 671–676

Hosokawa S, Moriyama S, Tomiyama A, Takada N (2003) PIV measurement of pressure distributions about single bubbles. J Nucl Sci Technol 40(10):754–762

Huhn F, Schanz D, Gesemann S, Schröder A (2016) FFT integration of instantaneous 3D pressure gradient fields measured by Lagrangian particle tracking in turbulent flows. Exp Fluids 57:151

Inoue O, Sakuragi A (2008) Vortex shedding from a circular cylinder of finite length at low Reynolds numbers. Phys Fluids 20:033601

Jakobsen M, Dewhirst T, Greated C (1997) Particle image velocimetry for predictions of acceleration fields and forces within fluid flows. Meas Sci Technol 8:1502–1516

Jaw S, Chen J, Wu P (2009) Measurement of pressure distribution from PIV experiments. J Vis 12:27–35

Jeong J, Hussain F (1995) On the identification of a vortex. J Fluid Mech 285:69

Laskari A, de Kat R, Ganapathisubramani B (2016) Full-field pressure from snapshot and time-resolved volumetric PIV. Exp Fluids 57:44

Liu X, Katz J (2006) Instantaneous pressure and material acceleration measurements using a four-exposure PIV system. Exp Fluids 41:227–240

Lynch K, Scarano F (2014) Material acceleration estimation by four-pulse tomo-PIV. Meas Sci Technol 25:084005

Marzouk O, Nayfeh A, Akhtar I, Arafat H (2007) Modeling steady-state and transient forces on a cylinder. J Vib Control 13(7):1065–1091

McClure J, Morton C, Yarusevych S (2015) Flow development and structural loading on dual step cylinders in laminar shedding regime. Phys Fluids 92:455–470

McClure J, Yarusevych S (2016) Vortex shedding and structural loading characteristics of finned cylinders. J Fluids Struct 10:100–101

Moin P, Mahesh K (1998) Direct numerical simulation: a tool in turbulence research. Annu Rev Fluid Mech 30:539–578

Morton C, Yarusevych S (2010) Vortex shedding in the wake of a step cylinder. Phys Fluids 22:083602

Murai Y, Nakada T, Suzuki T, Yamamoto F (2007) Particle tracking velocimetry applied to estimate the pressure field around a Savonius turbine. Meas Sci Technol 18:2491–2503

Neeteson N, Rival R (2015) Pressure-field extraction on unstructured flow data using a Voronoi tessellation-based networking algorithm: a proof-of-principle study. Exp Fluids 56:44

Norberg C (2003) Fluctuating lift on a circular cylinder: review and new measurements. J Fluids Struct 17:57–96

Novara M, Scarano F (2013) A particle-tracking approach for accurate material derivative measurements with tomographic PIV. Exp Fluids 54:1584

Pan Z, Whitehead J, Thompson S, Truscott T (2016) Error propagation dynamics of PIV-based pressure field calculations: how well does the pressure Poisson solver perform inherently?". arXiv:1602.00037 [physics.flu-dyn]

Persillon H, Braza M (1998) Physical analysis of the transition to turbulence in the wake of a circular cylinder by three-dimensional NavierStokes simulation. J Fluid Mech 365:23–88

Pröbsting S, Scarano F, Bernardini M, Pirozzoli S (2013) On the estimation of wall pressure coherence using time-resolved tomographic PIV. Exp Fluids 54:1567

Ragni D, van Oudheusden BW, Scarano F (2012) 3D pressure imaging of an aircraft propeller blade-tip flow by phase-locked stereoscopic PIV. Exp Fluids 52:463–477

Regert T, Chatellier L, Tremblais B, David L (2001) Determination of pressure fields from time-resolved data. In: 9th International symposium on particle image velocimetry. Tsukuba, Japan

Roshko A (1993) Perspectives of bluff body aerodynamics. J Wind Ind Aerodyn 49:79–100

Scarano F, Poelma C (2009) Three-dimensional vorticity patterns of cylinder wakes. Exp Fluids 47(1):69–83

Schanz D, Gesemann S, Schröder A (2016) Shake-The-Box: Lagrangian particle tracking at high particle image densities. Exp Fluids 57:70

Schneiders J, Pröbsting S, Dwight R, van Oudheusden B, Scarano F (2016) Pressure estimation from single-snapshot tomographic PIV in a turbulent boundary layer. Exp Fluids 57:53

Sciacchitano A, Wieneke B (2016) PIV uncertainty propagation. Meas Sci Technol 27:084006

Trefethen L (2000) Spectral methods in Matlab. SIAM, Philadelphia

Tronchin T, David L, Farcy A (2015) Loads and pressure evaluation of the flow around a flapping wing from instantaneous 3D velocity measurements. Exp Fluids 56:1870

van Oudheusden B (2013) PIV-based pressure measurement. Meas Sci Technol 24:032001

van Oudheusden B, Scarano F, Casimiri E (2006) Non-intrusive load characterization of an airfoil using PIV. Exp Fluids 40:988–992

van Oudheusden B, Scarano F, Roosenboom E, Casimiri E, Souverein L (2007) Evaluation of integral forces and pressure fields from planar velocimetry data for incompressible and compressible flows. Exp Fluids 43:153–162

Violato D, Moore P, Scarano F (2011) Lagrangian and Eulerian pressure field evaluation of rod-airfoil flow from time-resolved tomographic PIV. Exp Fluids 50:1057–1070

Wieselsberger C (1921) New data on the law of hydro and aerodynamic resistance. Phys Z 22:321–328

Williamson C (1989) Oblique and parallel modes of vortex shedding in the wake of a circular cylinder at low Reynolds numbers. J Fluid Mech 206:579

Williamson C (1996) Vortex dynamics in the cylinder wake. Annu Rev Fluid Mech 28:477–539

Wissink J, Rodi W (2008) Numerical study of the near wake of a circular cylinder. Int J Heat Fluid Flow 29:1060–1070

Zhao M, Cheng L (2014) Vortex-induced vibration of a circular cylinder of finite length. Phys Fluids 26:015111